Energy & Environmental Science

ROYAL SOCIETY OF CHEMISTRY

PAPER

View Article Online
View Journal | View Issue



Cite this: *Energy Environ. Sci.*, 2022, **15**, 727

# Dynamics and control of active sites in hierarchically nanostructured cobalt phosphide/chalcogenide-based electrocatalysts for water splitting†

Yonggui Zhao, [a] Nanchen Dongfang,[a] Carlos A. Triana, [a] Chong Huang,[a] Rolf Erni, [b] Wenchao Wan, [a] Jingguo Li, [a] Dragos Stoian, [c] Long Pan, [d] Ping Zhang,[e] Jinggang Lan, [a] Marcella Iannuzzi [a] and Greta R. Patzke *[a]

The rational design of efficient electrocatalysts for industrial water splitting is essential to generate sustainable hydrogen fuel. However, a comprehensive understanding of the complex catalytic mechanisms under harsh reaction conditions remains a major challenge. We apply a self-templated strategy to introduce hierarchically nanostructured "all-surface" Fe-doped cobalt phosphide nanoboxes (Co@CoFe–P NBs) as alternative electrocatalysts for industrial-scale applications. *Operando* Raman spectroscopy and X-ray absorption spectroscopy (XAS) experiments were carried out to track the dynamics of their structural reconstruction and the real catalytically active intermediates during water splitting. Our *operando* analyses reveal that partial Fe substitution in cobalt phosphides promotes a structural reconstruction into P–Co–O–Fe–P configurations with low-valence metal centers ($M^0/M^+$) during the hydrogen evolution reaction (HER). Results from density functional theory (DFT) demonstrate that these *in situ* reconstructed configurations significantly enhance the HER performance by lowering the energy barrier for water dissociation and by facilitating the adsorption/desorption of HER intermediates (H*). The competitive activity in the oxygen evolution reaction (OER) arises from the transformation of the reconstructed P–Co–O–Fe–P configurations into oxygen-bridged, high-valence $Co^{IV}$–O–$Fe^{IV}$ moieties as true active intermediates. In sharp contrast, the formation of such $Co^{III/IV}$–O–$Fe^{III/IV}$ moieties in Co–FeOOH is hindered under the same conditions, which outlines the key advantages of phosphide-based electrocatalysts. *Ex situ* studies of the as-synthesized reference cobalt sulfides (Co–S), Fe doped cobalt selenides (Co@CoFe–Se), and Fe doped cobalt tellurides (Co@CoFe–Te) further corroborate the observed structural transformations. These insights are vital to systematically exploit the intrinsic catalytic mechanisms of non-oxide, low-cost, and robust overall water splitting electrocatalysts for future energy conversion and storage.

Received 20th July 2021,
Accepted 3rd December 2021

DOI: 10.1039/d1ee02249k

rsc.li/ees



## Broader context

Water splitting to generate clean hydrogen is a promising strategy for future energy conversion and storage systems. Transition metal chalcogenides (TMCs) and phosphides (TMPs) have emerged as excellent candidates to promote the overall efficiency of water splitting. However, the underlying structural reconstructions of TMPs/TMCs that give rise to their high electrocatalytic performance still remain to be understood. This calls for the determination of their real catalytically active species through advanced *operando* characterization techniques which monitor their structural reconstruction dynamics and provide insights into the intrinsic catalytic mechanisms. In this work, we constructed a series of tailored TMP/TMC nano-architectures for overall water splitting applications. We present in-depth mechanistic insights into the hydrogen evolution reaction (HER) and oxygen evolution reaction (OER) processes of the as-prepared cobalt phosphide-based nanobox materials based on *operando* XAS and Raman spectroscopy, complemented with rotating ring disk electrode investigations. Furthermore, combination of DFT simulations with our *operando* studies sheds light on the crucial parameters for high HER and OER activities. This study highlights the importance of using *operando* techniques to capture structural reconstruction dynamics as the key to understanding intrinsic catalytic mechanisms.

[a] *Department of Chemistry, University of Zurich, Winterthurerstrasse 190, CH-8057 Zurich, Switzerland. E-mail: greta.patzke@chem.uzh.ch*
[b] *Electron Microscopy Center, Empa, Swiss Federal Laboratories for Materials Science and Technology, Überlandstrasse 129, CH-8600 Dübendorf, Switzerland*
[c] *Swiss-Norwegian Beamlines at the European Synchrotron Radiation Facility, 38000 Grenoble, France*
[d] *Key Laboratory of Advanced Metallic Materials of Jiangsu Province, School of Materials Science and Engineering, Southeast University, Nanjing 211189, China*
[e] *School of Electrical and Information Engineering and Key Laboratory of Advanced Ceramics and Machining Technology of Ministry of Education, Tianjin University, Tianjin 300072, China*

† Electronic supplementary information (ESI) available. See DOI: 10.1039/d1ee02249k

## Introduction

The development of efficient water electrolyzer systems is a promising approach to store renewable energy resources (*e.g.* sunlight and wind) in chemical commodities. To date, there are two general design concepts of water electrolyzers for industrial-scale applications, namely alkaline exchange membrane (AEM) electrolysis and proton exchange membrane (PEM) electrolysis.[1,2] AEM electrolyzers based on low-cost and earth-abundant elements meet practical applications rather directly, but their intrinsic barriers for accessing high current densities remain challenging. While PEM electrolyzers can achieve 3–4 times higher current densities than AEM electrolyzers, the use of noble metal electrocatalysts drives up their costs.[1] Therefore, the rational design of noble metal-free electrocatalysts with high current densities and robust electrochemical stability is crucial.[3–6]

Recent studies have demonstrated that transition metal chalcogenides (TMCs) and phosphides (TMPs) are promising candidates for AEM electrolyzers due to their high catalytic activities in both hydrogen evolution (HER, cathode) and oxygen evolution reactions (OER, anode).[7–14] However, TMPs and TMCs undergo structural reconstructions during electrolysis, which may in some cases affect their operational stability. To fully tap into the potential of noble metal-free TMCs and TMPs as overall water splitting electrocatalysts, intense efforts are required to understand their intrinsic catalytic mechanisms.[15–19] *Ex situ* investigations suggest that the structural reconstruction associated with oxygen incorporation in TMCs and TMPs is responsible for their high OER performance.[20–25] This reconstruction can proceed *via* two different routes. Either the as-prepared bulk compounds are fully oxidized into transition metal oxides or (oxy)hydroxides,[19,26–29] or their surfaces can reconstruct into core–shell structures with TMCs and TMPs remaining as core materials.[22,30–33]

In sharp contrast, the real active species in TMC- and TMP-based HER catalysts remain largely unknown, because their higher stability during HER makes it far more difficult to distinguish the active species from the bulk material, especially using standard *ex situ* techniques.[34–40] As the use of uniform materials as bifunctional electrocatalysts for overall water splitting is a promising industrial strategy, the HER dynamics of powerful dual TMC/TMP electrocatalysts needs to be understood. We thus focus on the *operando* identification of the real catalytically active species in both HER and OER driven by cobalt phosphide-based nanobox materials. Given that the as-synthesized TMC and TMP samples generally undergo oxidative changes during sample handling and transportation processes, time-resolved monitoring is essential.[3,41–46] Advanced *operando* techniques, such as XAS and Raman spectroscopy, have opened up new possibilities to capture the real active intermediates of electrochemical reactions,[19,47] which has brought forward notable progress in understanding the intrinsic catalytic mechanisms for a variety of electrocatalytic systems.[47–52]

High-surface nanomaterials are preferable targets for elucidating electrocatalytic interface processes.[53–56] Therefore, we constructed a series of hierarchical nanostructures of cobalt phosphide nanoboxes (denoted as Co–P NBs) and Fe doped cobalt phosphide nanoboxes (Co@CoFe–P NBs) from tailored coordination polymer precursors *via* a self-templating strategy. This controllable strategy furthermore brought forward single-shell cobalt sulfide nanoboxes (Co–S NBs), hybrids of cobalt sulfides and CoFe-based Prussian blue nanoboxes (Co–S@CoFe–PB NBs), double-shell CoFe-based oxide nanoboxes (Co@CoFe–O NBs), as well as CoFe-based selenides (Co@CoFe–Se), and CoFe-based tellurides (Co@CoFe–Te).

Among all these prepared nanostructured materials, the as-synthesized Co@CoFe–P NBs exhibit the best HER and OER performances over a wide pH range (0–14), along with robust electrochemical stability over 220 h in overall water splitting. Furthermore, *operando* XAS and Raman spectra in combination with rotating ring-disk electrode (RRDE) techniques unraveled the structural reconstruction dynamics and the intrinsic catalytic mechanisms of the as-prepared Co–P NBs and Co@CoFe–P during both the HER and OER processes.

Our *operando* results show that the high HER activities of Co–P (Co@CoFe–P) NBs arise from their *in situ* reconstruction into P–Co–O (P–Co–O–Fe–P) configurations with low-valence metal centers ($M^0/M^+$). Furthermore, the newly formed oxygen-bridged $Co^{IV}$–O–$Co^{IV}$ and $Co^{IV}$–O–$Fe^{IV}$ moieties are the active OER sites of the as-prepared Co–P and Co@CoFe–P NBs, respectively, and their formation was found to be far more facile than in Co/Fe-oxyhydroxide catalysts. Related restructuring trends were corroborated for Co–S, Co@CoFe–Se, and Co@CoFe–Te catalysts before and after electrolysis. Furthermore, density functional theory (DFT) calculations provide a detailed mechanistic background for these key *in situ* structural reconstructions of nanoscale cobalt phosphide and chalcogenide electrocatalysts.

## Results and discussion

### Materials synthesis and characterization

First, ZIF-67 nanocubes (NCs) were synthesized at room temperature based on slightly modified protocols from previous reports[57–60] (Fig. 1a, e and Fig. S1 and experimental details in the ESI†) and were characterized using a wide range of techniques (Fig. S2–S4, ESI†). The as-prepared ZIF-67 NCs were then converted into the core–shell architecture of ZIF-67@CoFe–PB NCs *via* a convenient anion-exchange approach between $Fe(CN)_6^{3-}$ from $K_3Fe(CN)_6$ and $C_4H_5N_2^-$ starting from ZIF-67 (see experimental and analytical details in the ESI,† Fig. S1, S5–S9 and detailed discussion in Fig. S5). FESEM and TEM images (Fig. 1b, f and Fig. S6, ESI†) illustrate that the as-prepared ZIF-67@CoFe–PB NCs exhibit similar cubic morphologies compared with that of pristine ZIF-67 NCs. Moreover, a narrow void between the inner core and the outer shell is clearly visible for a representative nanoparticle, indicating the formation of yolk–shell architectures in ZIF-67@CoFe–PB NCs (Fig. 1f and Fig. S6d, ESI†). To investigate the spatial distribution of different elements and to confirm the formation of yolk–shell features, STEM-EDX line-scans and element mappings (Fig. 1j and Fig. S8, ESI†) were carried out

 

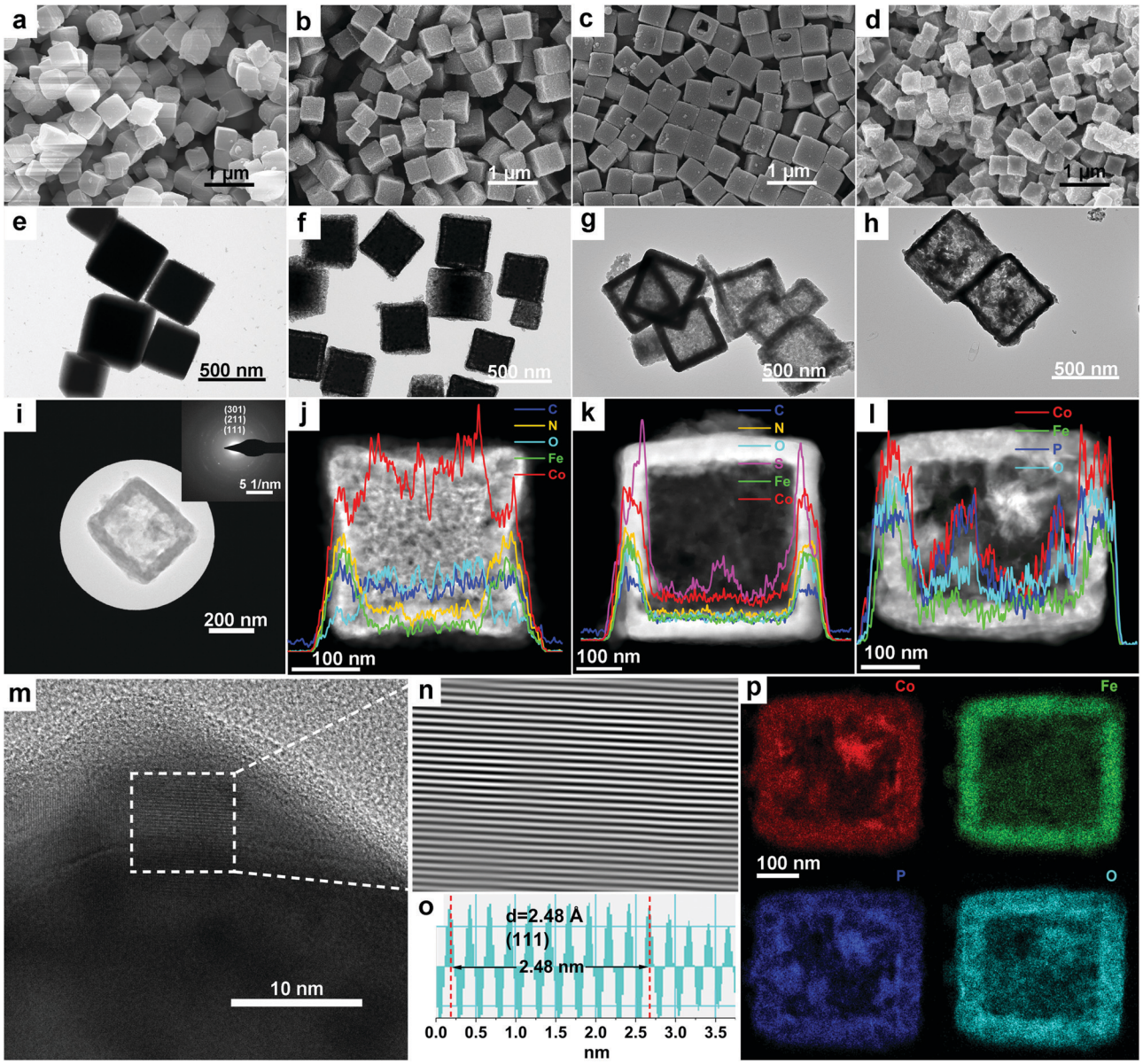


Fig. 1 FESEM and TEM images of: (a and e) ZIF-67 nanocubes, (b and f) ZIF-67@CoFe–PB nanocubes, (c and g) Co–S@CoFe–PB nanoboxes, and (d and h) Co@CoFe–P nanoboxes. (i) High-resolution transmission electron microscopy (HR-TEM) image and the corresponding SAED pattern. (j–l) High-angle annular dark field-scanning transmission electron microscopy (HAADF-STEM) images and STEM-EDX line-scan profiles of ZIF-67@CoFe–PB nanocube, Co–S@CoFe–PB nanobox, and Co@CoFe–P nanobox particles. (m–o) HR-TEM image, corresponding inverse fast Fourier transformation (IFFT) image and line scan profile of a Co@CoFe–P nanobox particle. (p) STEM-EDX element mappings of Co@CoFe–P nanobox particles (red = Co, green = Fe, blue = P, cyan = O).

for an individual yolk–shell particle. As shown in Fig. 1j, the element distributions of Co and Fe are dispersed over the entire cuboidal particle. However, the distribution of Co displays a distinct convex trend with more intense signals from the core. In contrast, a concave tendency with a higher signal intensity from the shell is observed for the distribution of Fe. All these observations strongly support the successful formation of core–shell nanostructures of ZIF-67@CoFe–PB NCs.

Hierarchically nanostructured Co–S@CoFe–PB NBs were fabricated by using the as-obtained yolk–shell ZIF-67@CoFe–PB NCs as templates *via* a hydrothermal reaction with TAA at 120 °C (see experimental details in the ESI†). Furthermore, a wide range of characterization methods was employed to investigate the structural and morphological properties of the as-synthesized Co–S@CoFe–PB NBs (Fig. 1c, g, k and Fig. S5, S10–S13, ESI†). Based on our recent work and on previous studies on ZIF-67,[21,34,61–63] the formation of Co–S@CoFe–PB NBs can be basically explained with an anion-exchange reaction between $S^{2-}$ from TAA and $C_4H_5N_2^-$ from ZIF-67 during the sulfidation reaction (discussion and details in Fig. S5 and S11, ESI†). It should be pointed out that the chemical exchange between $S^{2-}$ and $CN^-$ in CoFe–PB can be neglected under the

conditions applied in this study, mainly due to the insufficient kinetics at lower temperature and with the limited reaction time.[62,64] As shown in Fig. 1k, STEM-EDX line-scan analysis of Co–S@CoFe–PB indicates a distinct elemental distribution of S within the shell. As expected, the inner layer of the shell displays intense S signals compared to the outer layer of the shell, suggesting the formation of hierarchically nanostructured cubes of Co–S@CoFe–PB NBs. Specifically, the newly formed Co–S species were mainly present in the inner layer of the shells, while the unreacted CoFe–PB compounds were preserved in the outer layer of the shell (Fig. 1k and Fig. S12, ESI†).

Hierarchical Co@CoFe–P NBs were obtained using a simple chemical vapor deposition method using $NaH_2PO_2$ as the phosphor source under Ar atmosphere (see experimental details in the ESI†). After phosphorization of the yolk–shell ZIF-67@CoFe–PB NC precursors with optimized experimental parameters, the as-prepared Co@CoFe–P NBs exhibit a well-defined hierarchical nanobox morphology (Fig. 1d and h). It was observed that both the amounts of $NaH_2PO_2$ and the phosphorization temperature influenced the morphologies of the final products (Fig. S17–S27, discussion and details in Fig. S21, and details in Discussion I, ESI†). Well-defined hierarchical nanobox architectures were achieved through the optimized experimental parameters with a mass ratio of 1 : 20 between ZIF-67@CoFe–PB NCs and $NaH_2PO_2$ reacted at 350 °C for 2 h (Fig. 1d, h and Fig. S18m–p, ESI†). The SAED pattern of optimized Co@CoFe–P NBs (Fig. 1i) shows three characteristic diffraction rings, corresponding to the main exposed crystal planes (111), (211), and (301) of CoP (PDF No. 29-0497, S. G. *Pnma*), which agrees with the PXRD patterns (Fig. S24, ESI†). HR-TEM and the corresponding inverse fast Fourier transform (IFFT) images (Fig. 1m–o and Fig. S19, ESI†) of Co@CoFe–P NBs manifest a clear inter-planar spacing of 2.48 Å, which is assigned to the exposed (111) crystal plane of CoP (PDF No. 29-0497, S. G. *Pnma*). STEM-EDX line-scan analysis and element mappings (Fig. 1l and p) of Co@CoFe–P NBs illustrate that Co, P, and O are distributed in the inner and outer shells of the box-shaped particle, while Fe is mainly detected in the shell. The presence of O signals (Fig. 1l and p) is in principle due to the inevitable oxidation of P upon exposure to air.[22,65–70] These results in their entirety support that the as-synthesized yolk–shell ZIF-67@CoFe–PB NC precursors are converted after phosphorization into hierarchical architectures of Co@CoFe–P NBs.

To further explore the impact of different cations or anions on the structural and morphological properties of the coordination polymer precursors, Co–S NBs, Co–PB NCs, Co–P NBs, Fe-PB NCs, Fe-P NBs, CoFe–PB NCs, CoFe–P NBs, Co@CoFe–O NBs, Co@CoFe–Se, and Co@CoFe–Te were prepared as well (see experimental details in the ESI†). According to our results, a distinct single-shell nanobox morphology was obtained for Co–S NBs (Fig. S14–S16, ESI†). Co–P, Fe–P, and CoFe–P NBs retain the initial cubic morphology but feature thicker shells (Fig. S28–S39, ESI†). As shown in Fig. S40–S42 (ESI†), the as-prepared Co@CoFe–O NBs show a well-defined double-shell nanobox architecture. In contrast, the cubic morphology cannot be preserved in the presence of Se and Te, shown in Fig. S43–S46 (ESI†).

### *Ex situ* XAS characterization

The local coordination environments and electronic properties of the Co and Fe centers for the investigated catalysts were explored using *ex situ* X-ray absorption spectroscopy (XAS) (Fig. 2 and Fig. S47–S51, ESI†). To understand the effects of sulfidation on the electronic structure of ZIF-67@CoFe–PB NCs, *ex situ* XAS data were recorded for the samples before and after sulfidation (discussion and details in Fig. S47, ESI†). From the XAS investigations, we further corroborate that the anion-exchange reaction in Co–S@CoFe–PB NBs mainly occurred between $S^{2-}$ from TAA and $C_4H_5N_2^-$ from ZIF-67.

Fig. 2a presents *ex situ* Co K-edge X-ray absorption near-edge structure (XANES) spectra of Co–P NBs, Co@CoFe–P NBs, Co@CoFe–O NBs, and the references Co foil, $Co(OH)_2$, Co–FeOOH, $Co_3O_4$, and CoOOH. The rising absorption edge position of Co–P NBs is lower than that of $Co(OH)_2$ but higher than that of Co foil, suggesting that the average valence state of Co centers in Co–P NBs is slightly lower than +2.[12,23,59,66] To further explore the local electronic structure of the as-prepared catalysts, the XANES spectrum of Co–P NBs was calculated using *ab initio* finite difference methods using the model structure defined in the PDF card No. 29-0497 (S. G. *Pnma*) as shown in Fig. S48 (ESI†). Based on the XANES simulation results (Table S5, discussion and details in Fig. S48 and S49, ESI†), we conclude that the local coordination environments of Co ions in Co–P NBs originate from the asymmetric configuration of Co–$P_{6-x}O_x$ moieties. The XAS data of Co@CoFe–P NBs (Fig. 2a and b) are similar to those of Co–P

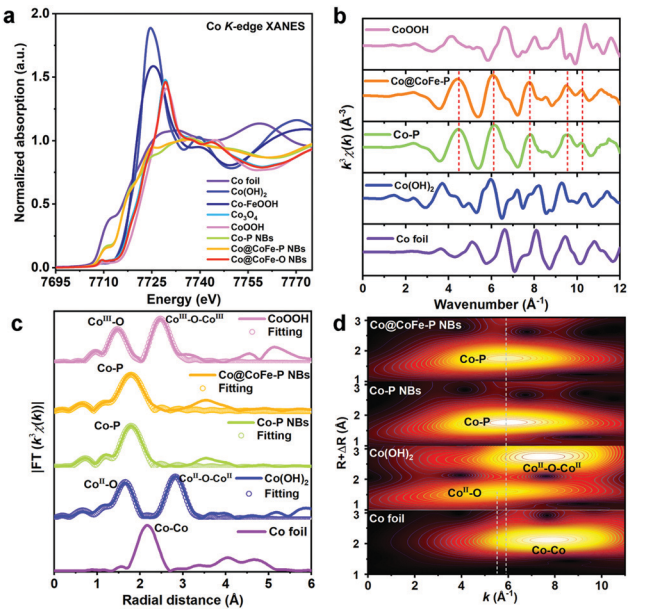


Fig. 2 (a) Co K-edge XANES spectra of as-synthesized samples *vs.* references. (b) Co K-edge EXAFS spectra of the as-synthesized samples *vs.* references. (c) Fitting of the Co K-edge FT-EXAFS spectra of the as-synthesized samples *vs.* references. (d) Co K-edge WT contour profiles of the as-synthesized samples *vs.* references.

NBs except for a slight increase in the peak intensity at ~7725 eV (XANES, Fig. 2a), suggesting an increased coordination number (CN) of Co–O bonds (denoted as $CN_{Co-O}$) in Co@CoFe–P NBs. Based on previous reports,[25,71–73] partial substitution of Co by Fe can weaken the orbital affinity for the 3d electrons and regulate the occupation of metal valence states, thus, lowering the energy barrier for the formation of M–O (M = Co, Fe) bonds. $CN_{Co-O}$ and $CN_{Co-P}$ in Co–P NBs were calculated to be 0.30 and 5.79, respectively, from fitting of the FT-EXAFS spectra (Fig. 2c and Table S5, ESI†). As expected, the as-prepared Co@CoFe–P NBs exhibit an increased $CN_{Co-O}$ of 0.61 and a decreased $CN_{Co-P}$ value of 5.29. These results are also evident in the wavelet transform (WT) of the EXAFS spectra (Fig. 2d), where the as-prepared Co@CoFe–P NBs show weaker signals in the intensity maximum at around 5.91 $Å^{-1}$ (first Co–P coordination shell) compared with Co–P NBs. The Fe K-edge XAS data also display analogous features, evidencing the presence of asymmetric Co/Fe-$P_{6-x}O_x$ moieties in the as-prepared Co@CoFe–P NBs (discussion and details in Fig. S50, ESI†). For comparison, the local atomic configurations of Co@CoFe–O NBs were also explored and they implied that the as-prepared oxide sample maintained a spinel-type crystal structure (discussion and details in Fig. S51, ESI†).

To unravel the surface chemical compositions of the as-synthesized samples, X-ray photoelectron spectroscopy (XPS) analyses were further carried out, and these results are also in agreement with the above XAS results (discussion and details in Fig. S52 and S53, ESI†).

## Electrocatalytic performance

Their favorable intrinsic gas/ion-diffusion capability, their adequate interface for electrolyte penetration, and their tuneable electronic structure render the as-synthesized hierarchically hollow Co@CoFe–PB nanobox architectures[32,35,57,59,61] promising candidates for efficient water splitting. To optimize the electrocatalytic performance of Co@CoFe–P NBs, the effects of synthetic parameter variations (*e.g.* $NaH_2PO_2$ amounts and reaction temperatures) on the catalytic performance were investigated first. The extrinsic influence of Ohmic contact resistance was eliminated with a 90% iR drop correction for all the investigated working electrodes (Fig. S54, ESI†).[55,74,75] Measurement results (Fig. S55–S58, ESI†) show that the catalysts prepared at 350 °C with 400 mg of $NaH_2PO_2$ display the best electrocatalytic activities.

**HER activity at pH 0.** We first performed HER tests for the as-prepared catalysts obtained under optimized synthetic parameters in 0.5 M $H_2SO_4$ (Fig. 3a, b and Fig. S59, ESI†). To assess the productive influence of the as-constructed hierarchical nanostructures and the phosphide introduction on the HER performance, Co–P NB, Fe–P NB, CoFe–P NB, and Co@CoFe–O NB reference electrodes were fabricated and tested under the same conditions. As shown in Fig. 3a, an increase in the HER activity from Co@CoFe–O, Co–P, Fe–P, and further to Co@CoFe–P NBs was observed in 0.5 M $H_2SO_4$. More specifically, to deliver a geometric current density of 10 mA $cm^{-2}$, a minimum overpotential value of 83 mV was required for Co@CoFe–P NBs, which clearly outperformed those of

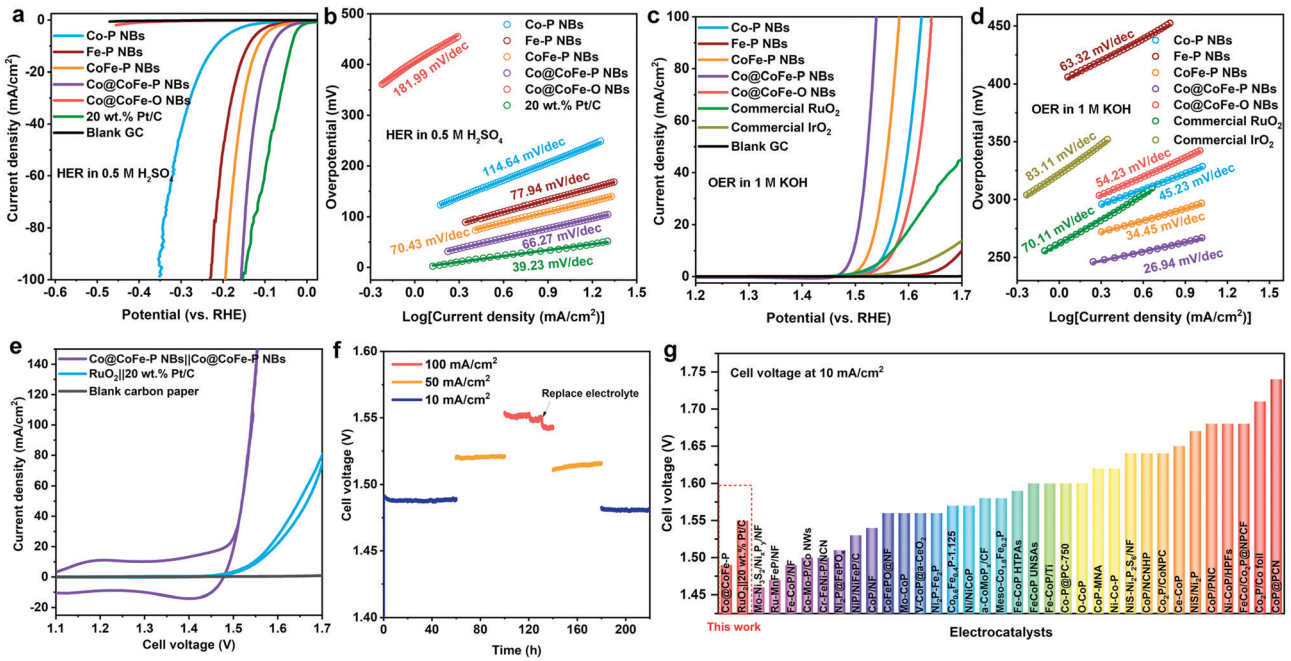


Fig. 3 (a and c) Linear sweep voltammetry (LSV) curves with a scan rate of 5 mV $s^{-1}$ at room temperature and (b and d) Tafel plots of the as-prepared Co–P NBs, Fe–P NBs, CoFe–P NBs, Co@CoFe–P NBs, and Co@CoFe–O NBs *vs.* commercial reference catalysts in 0.5 M $H_2SO_4$ (pH 0.2) for HER and 1.0 M KOH (pH 13.8) for OER, respectively. (e) Cyclic voltammetry (CV) curves of a two-electrode system assembled with Co@CoFe–P NBs||Co@CoFe–P NBs and $RuO_2$||20 wt% Pt/C electrocatalysts in 1.0 M KOH. (f) Stability measurements of Co@CoFe–P NBs||Co@CoFe–P NBs loaded on carbon paper. (g) Summary of recent representative studies of overall water splitting electrocatalysts with their corresponding cell voltage at a current density of 10 mA $cm^{-2}$ (Table S13, ESI†).

CoFe–P (116 mV), Fe–P (140 mV), Co–P (217 mV), and Co@CoFe–O NBs (406 mV at 1 mA $cm^{-2}$). An additional overpotential of 46 mV was essential for Co@CoFe–P NBs to compete with the HER activity of commercial 20 wt% Pt/C at a current density of 10 mA $cm^{-2}$. However, when the current density is close to 100 mA $cm^{-2}$, the as-synthesized Co@CoFe–P NBs are a clear competitor for replacing commercial 20 wt% Pt/C in industrial-scale hydrogen production under acidic conditions (Fig. 3a). For obtaining detailed insight into the HER kinetics of the as-prepared catalysts in 0.5 M $H_2SO_4$, Tafel slope values are depicted in Fig. 3b. Co@CoFe–P NBs exhibit a more favorable Tafel slope value of 66.27 mV $dec^{-1}$, superior to those of CoFe–P (70.43 mV $dec^{-1}$), Fe–P (77.94 mV $dec^{-1}$), Co–P (114.64 mV $dec^{-1}$), and Co@CoFe–O (181.99 mV $dec^{-1}$), thus evidencing the faster HER kinetics for the formation of HER intermediates in Co@CoFe–P NBs. Moreover, the elaborate design of almost ''all-surface'' morphological metrics in Co@CoFe–P NBs can shorten the diffusion length of ions and thereby lead to faster charge transfer properties.[31,35,61,76] The results of electrochemical impedance spectroscopy (EIS) and chronopotentiometry measurements further demonstrate the enhanced electron transfer properties and good stabilities of the as-prepared Co@CoFe–P NBs (discussion and details in Fig. S59, ESI†).

**HER activity in the pH range from 7–14.** Furthermore, we measured the HER performances of Co@CoFe-NBs at different pH values (1.0 M KOH and 1.0 M PBS) (Fig. S60 and S64a, c, e, ESI†). As expected, the as-prepared Co@CoFe-NBs also show excellent HER performance with an overpotential of 104 mV (150 mV) at a current density of 10 mA $cm^{-2}$, a Tafel slope value of 79.0 mV $dec^{-1}$ (90.0 mV $dec^{-1}$), and a charge transfer resistance of 19.84 Ω (70.73 Ω), along with electrochemical stability for 1000 CVs and over 12 h at current densities of 10 and 20 mA $cm^{-2}$ in 1.0 M KOH (1.0 M PBS) (Fig. S60, ESI†). Interestingly, the as-prepared Co@CoFe–P NB electrode competes favourably with commercial 20 wt% Pt/C at much lower current densities of 15 mA $cm^{-2}$ and 50 mA $cm^{-2}$ in 1.0 M PBS and 1.0 M KOH, respectively (Fig. S60a and e, ESI†). Moreover, the HER activities obtained in Co@CoFe–P NBs also outmatch most recent state-of-the-art HER electrocatalysts (Table S11, ESI†). FESEM and TEM investigations (Fig. S66 and S67, ESI†) clearly demonstrate that the as-prepared Co@CoFe–P NBs largely preserve their initial morphology after long-time measurements. All of the above results corroborate the benefits of engineering hierarchically nanostructured Co@CoFe–P NBs as high-performance HER electrocatalysts.

**OER activity.** Another prerequisite for overall water splitting electrocatalysts is excellent OER activity.[59,66,69] Therefore, the as-prepared Co@CoFe–P NBs were further employed as anode materials and compared to benchmark catalysts (Fig. 3c, d and Fig. S64b, d, f, ESI†). The overall OER activities of the as-investigated catalysts follow the order Co@CoFe–P > CoFe–P > Co–P > Co@CoFe–O > Fe–P (Fig. 3c). To reach a geometric current density of 10 mA $cm^{-2}$, the as-prepared Co@CoFe–P NBs only require a much lower overpotential of 266 mV, outperforming those of CoFe–P (296 mV), Co–P (327 mV), $RuO_2$ (340 mV), Co@CoFe–O (342 mV), $IrO_2$ (442 mV), and Fe–P (470 mV). The Tafel slopes of the as-prepared catalysts were also investigated and they underscored the accelerated OER kinetics from Fe–P over Co–P to Co@CoFe–P. As shown in Fig. 3d, Co@CoFe–P NBs exhibit the smallest Tafel slope value of 26.94 mV $dec^{-1}$, compared with CoFe–P (34.45 mV $dec^{-1}$), Co–P (45.23 mV $dec^{-1}$), Co@CoFe–O (54.23 mV $dec^{-1}$), Fe–P (63.32 mV $dec^{-1}$), $RuO_2$ (70.11 mV $dec^{-1}$), and $IrO_2$ (83.11 mV $dec^{-1}$). This indicates that Co@CoFe–P NBs display accelerated OER kinetics for the formation of OER intermediates (O*/OOH*) compared with the other investigated catalysts.[4,25,55] Furthermore, EIS tests were conducted for the investigated catalysts (Fig. S61a, ESI†), which demonstrated the favorable charge transfer mobility of the as-prepared Co@CoFe–P NBs during the OER. Moreover, the hierarchically nanostructured morphology offers a larger contact interface between the electrolyte and catalyst, thereby enabling a high density of exposed active sites to improve the OER activity.[25,32,59] To better assess the intrinsic OER activities of the as-synthesized catalysts, the electrochemical surface area (ECSA) was calculated to normalize the geometric current density (Fig. S62 and S63, ESI†). As expected, Co@CoFe–P NBs exhibit the highest double-layer capacitances ($C_{dl}$) along with improved intrinsic OER activity compared with Co–P NBs. This further indicates that Fe substitution can significantly promote the sluggish OER kinetics of Co–P NBs. The electrochemical stability of the as-prepared Co@CoFe–P electrode was checked using both CV cycling and chronoamperometry methods (Fig. S61b, ESI†). The results confirm that the elaborate nanostructured Co@CoFe–P NBs retain their initial OER activity after 1000 CVs and 12 h of chronopotentiometry measurements. Moreover, FESEM and TEM characterization studies further demonstrate the integrity of the initial cubic morphology in Co@CoFe–P NBs after the OER test (Fig. S68 and S69, ESI†). The excellent OER performance and stable morphological properties of Co@CoFe–P NBs render them competitive with most recent studies on non-noble metal OER electrocatalysts (Table S12, ESI†). For comparison, the HER activities over the whole pH range (0–14) and OER performances in 1.0 M KOH of the as-prepared Co–S NBs, Co–S@CoFe–PB NBs, Co@CoFe–Se, and Co@CoFe–Te were also measured (Fig. S70–S74, ESI†). Our results reveal that Co@CoFe–P NBs exhibit the best HER and OER activities of the listed chalcogenide electrocatalysts under comparable test conditions.

**Overall water splitting.** Inspired by the superior catalytic performance of Co@CoFe–P NBs under various pH conditions, we furthermore assembled a two-electrode system by employing Co@CoFe–P NBs as bifunctional electrodes for overall water splitting under alkaline conditions (Fig. 3e–g and Fig. S65, ESI†). Commercial $RuO_2$||20 wt% Pt/C electrodes were tested for comparison. As shown in Fig. 3e, the assembled Co@CoFe–P NB electrodes can deliver geometric current densities of 10 mA $cm^{-2}$ and 100 mA $cm^{-2}$ at very low cell voltages of 1.49 V and 1.54 V, respectively. These obtained cell voltages are substantially lower than for commercial $RuO_2$||20 wt% Pt/C and for most recently reported bifunctional electrocatalysts

 

(Fig. 3g and Table S13, ESI†). Furthermore, the long-term durability test verifies the superior electrochemical stability of Co@CoFe–P NBs, which maintains its initial catalytic activity for over 220 h (Fig. 3f) with only slight potential variations observed at a high current density of 100 mA $cm^{-2}$. Such excellent overall catalytic activity and high electrochemical stability render Co@CoFe–P NBs as an alternative candidate for low-cost and efficient water splitting in industrial applications. Moreover, the as-prepared Co–S@CoFe–PB NCs were tested for sodium-ion battery measurements, and they are also alternative materials for battery applications (discussion and details in Fig. S75, ESI†).

### Dynamics of active species derived from *operando* XAS

To probe the identity of the real catalytically active species and to understand the intrinsic structure–activity relationship during the water splitting half reactions, *ex situ* XPS and CV tests were first conducted on the investigated samples (Fig. S76 and S77 and details in Discussion II, ESI†). Our results indicate that the as-prepared phosphide materials undergo structural reconstruction during both HER and OER processes, which calls for the determination of the real active species involved in both reactions. To monitor the dynamic evolution of active species, we performed o*perando* XAS measurements on the as-prepared Co/Fe phosphide samples during HER and OER under alkaline conditions (see Experimental details in the ESI,† and Fig. S78).

**HER monitoring and dynamic role of Fe centers.** We first performed *operando* XAS tests to monitor the dynamics of active species on Co–P NBs during HER (Fig. S79 and S80, ESI†). Our results (see details in Discussion III, ESI†) reveal that the as-prepared Co–P NBs undergo structural reconstructions into P–Co–O moieties with low oxidation states of the Co centers ($Co^0/Co^+$).[12,77] These moieties act as true catalytically active species in HER. To explore the role of Fe substitution in the catalytic mechanisms of Co@CoFe–P NBs during HER, *operando* Co and Fe K-edge XAS data of Co@CoFe–P NBs were recorded (Fig. 4a–d and Fig. S81 and S82, ESI†). For Co@CoFe–P NBs immersed into the electrolyte (Fig. 4a and b), the increasing absorption edges of the Co K-edge XANES spectra shift to higher energy by ~0.27 eV, corresponding to an increase of the valence state of Co (by ~0.08), which is different from the negative energy shifts observed for Co–P NBs (Fig. S80a and b, ESI†). During cathodic polarization from 50 mV to −70 mV *vs.* RHE, Co@CoFe–P NBs show similar negative energy shifts in the increasing absorption edge as Co–P NBs with reduced peak intensities at 7727 eV, and a trend toward decreasing oxidation states of Co (Fig. 4a, b and Fig. S80a, b, ESI†). This suggests that Co@CoFe–P NBs operate *via* a very similar HER mechanism at their Co sites compared to Co–P NBs. The local coordination environments of Co centers in the as-prepared Co@CoFe–P NBs were further monitored with FT-EXAFS spectra. As shown in Fig. 4c, d and Fig. S81c (ESI†), the FT-EXAFS spectra of Co@CoFe–P NBs, immersed into the electrolyte, reveal the appearance of a distinctive second shell scattering at a radial distance of 2.85 Å, associated with the backscattering from Co–Co/Fe pairs, which indicates the formation of P–Co–O–Co/Fe–P configurations. These findings agree with the positive energy shifts observed in the increasing absorption edge of the XANES spectra (Fig. 4a). During cathodic polarization (Fig. 4c, d and Fig. S81c, ESI†), the intensity of the second scattering shell decreases as the applied potential

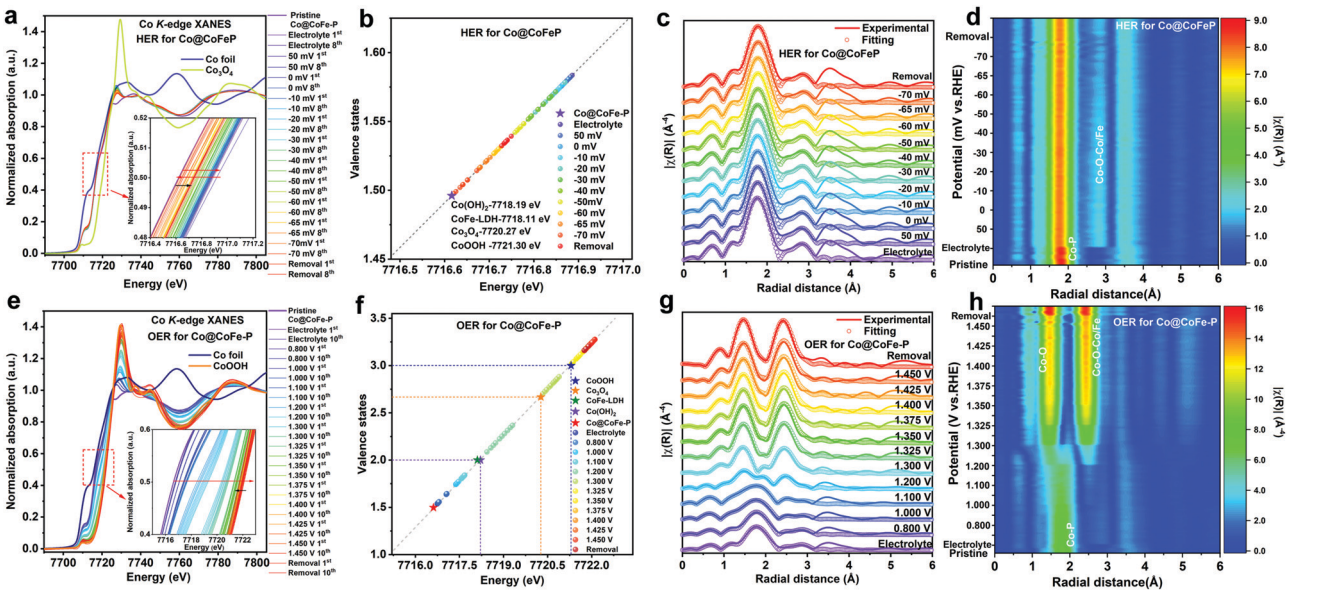


Fig. 4 (a and e) *Operando* Co K-edge XANES spectra of Co@CoFe–P recorded at different potentials in 1.0 M KOH for HER and OER. (b and f) Calculated Co valence states of Co@CoFe–P recorded at different potentials in 1.0 M KOH for HER and OER. (c and g) Fitting of *operando* Co K-edge FT-EXAFS spectra (merged) of Co@CoFe–P recorded at different potentials in 1.0 M KOH for HER and OER. (d and h) 2D contour plots of *operando* Co K-edge FT-EXAFS spectra of Co@CoFe–P recorded at different potentials in 1.0 M KOH for HER and OER. (Note: when the potential is higher than the onset potential for OER (HER), the formation of gas bubbles drastically influences the quality of EXAFS data recorded in the transmission mode. Therefore, we only present the XANES data without showing the EXAFS data when there was a more intense gas evolution.)

increases, but thereafter, it increases after the removal of the applied cathodic potential. This suggests that the P–Co–O–Co/Fe–P configurations are structurally flexible during the HER. From the fitting of *operando* FT-EXAFS spectra (Fig. 4c and Table S8, ESI†), we observe that both $CN_{Co-O}$ and $CN_{Co-Co/Fe}$ constantly decrease, correspondingly the mean bond distances of Co–O and Co–Co/Fe slightly increase. However, both the $CN_{Co-P}$ and the mean bond distance of Co–P remain almost identical during cathodic polarization. Based on these results, we suggest that the *in situ* reconstructed P–Co–O–Co/Fe–P configurations play a pivotal role in the HER activity of Co@CoFe–P NBs. Unfortunately, it is challenging to distinguish the scattering difference between second shells of Co–Fe and Co–Co paths based on Co K-edge XAS data. The quite low Fe to Co ratio in Co@CoFe–P NBs (Table S3, ESI†) makes it reasonable to propose that most Fe atoms interact with Co atoms *via* bridging O atoms. The plausible formation of P–Co–O–Fe–P configurations in Co@CoFe–P NBs can be evaluated from Fe K-edge XAS data.[46,78,79] Results from *operando* Fe K-edge FT-EXAFS spectra (Fig. S82 and see details in Discussion IV, ESI†) indicate the appearance of a prominent second scattering shell at 2.82 Å, supporting the occurrence of P–Co–O–Fe–P configurations in Co@CoFe–P NBs during the HER process. We also observed that the *in situ* reconstructed P–Co–O–Fe–P configurations undergo structural changes after removing the applied potential, which agrees with the observations from the Co K-edge XANES spectra. Moreover, the changes in the Fe oxidation states are more apparent compared with those of Co (Fig. 4b and Fig. S82b, ESI†), indicating the important role of Fe in Co@CoFe–P NBs during HER.

**Intrinsic HER mechanism.** From our *operando* XAS data, we conclude that the real catalytically active species in Co@CoFe–P NBs for HER arise from the *in situ* reconstructed P–Co–O–Fe–P moieties with low valence states of the metal centers ($M^0/M^+$). Compared with the Co sites, the Fe sites in the P–Co–O–Fe–P moieties are more active toward $OH^-/H_2O$ adsorption due to their greater changes in oxidation states during the HER process (Fig. 4b and Fig. S82b, ESI†).[9,48] Additionally, the *operando* XAS results for Co–P NBs (Fig. S79, S80 and details in Discussion III, ESI†) reveal that the formation of P–$Co^{II}$–O–$Co^{II}$–P configurations during the HER is barely detectable when compared with Co@CoFe–P NBs. This explains why the reconstructed P–Co–O–Fe–P moieties enable an enhanced HER activity of Co@CoFe–P NBs compared with Co–P NBs (featuring P–Co–O moieties) (Fig. S60a–c, ESI†).

**OER monitoring and dynamic role of Fe centers.** We also performed *operando* XAS analyses to investigate the structural reconstruction and the catalytic OER mechanism of the as-prepared phosphide-based catalysts (Fig. 4e–h and Fig. S83–S86, ESI†). Our *operando* results indicated that the real OER active species of Co–P NBs originate from the *in situ* reconstructed $Co^{IV}O_2$ species (Fig. S83, S84 and see details in Discussion V, ESI†). The role of Fe centers in the catalytic OER mechanism was further investigated by *operando* XAS on Co@CoFe–P NBs. As shown in Fig. 4e and f, when compared to the HER tests, similar changes in the XANES spectra were observed upon immersion of the electrodes into the electrolyte (Fig. 4a, b, e, f and Fig. S82a, b and S86a, b, ESI†): (i) increased oxidation states of Co and Fe, and (ii) enhanced peak intensities at ~7130 eV and ~7727 eV, respectively, which indicates the formation of $Co^{II}$–O–$Fe^{II}$ moieties. During anodic polarization, the energy positions of the rising absorption edges of both Co and Fe K-edge XANES spectra are shifted to higher energy (Fig. 4e and Fig. S86a, ESI†), implying the oxidation of both metal centers. The maximum values of oxidation states for Co and Fe are +3.28 and +3.18, respectively, appearing at an applied anodic potential of 1.450 V *vs.* RHE (Fig. 4f and Fig. S86b, ESI†). After removing the applied potential, the oxidation states of Co and Fe further decreased to +3.17 and +3.11, respectively, suggesting their partial redox reversibility after the OER (Fig. 4f and Fig. S86b, ESI†). It is noteworthy that the oxidation state of Co can reach +3 at a lower anodic potential of 1.325 V *vs.* RHE in Co@CoFe–P NBs (Fig. 4f) than for Co–P NBs (1.4 V *vs.* RHE in Fig. S84b, ESI†). This demonstrates that partial Fe substitution can facilitate the oxidation of Co ions.[44,46,78]

**Dynamic interaction of Co and Fe centers in the OER.** The local electronic structure and the dynamics of active catalytic species in Co@CoFe–P NBs during OER were further evaluated from *operando* EXAFS spectra (Fig. 4g, h and Fig. S85b, c, S86c, d, ESI†). In agreement with our results for Co–P NBs (Fig. S83 and S84, ESI†), similar changes in the coordination environments of Co and Fe centers are also observed in Co@CoFe–P NBs (Fig. 4g, h and Fig. S85b, c, S86c, d, Discussion VI, ESI†). For samples immersed into the electrolyte, a second shell scattering peak appears in the Co and Fe K-edge FT-EXAFS spectra, arising from the backscattering of $Co^{II}$–$Fe^{II}$ pairs (Fig. 4g, h and Fig. S86c, d, ESI†). At an anodic potential of 1.0 V *vs.* RHE, the Co K-edge FT-EXAFS spectra display a lower scattering peak intensity of the $Co^{II}$–$Fe^{II}$ pairs, and a new peak arising from $Co^{III}$–$Co^{III}$ scattering is detected at 2.52 Å (Fig. 4g, h and Fig. S85c, ESI†).[80–82] For the potential range from 1.2 V to 1.3 V *vs.* RHE, the second shell scattering peak becomes broader, which is due to the formation of $Co^{III}$–O–$Fe^{III}$ moieties. The scattering from Co–P bonds disappears above 1.325 V *vs.* RHE, and only the scattering from $Co^{III}$–O bonds remains in the first shell. Likewise, the formation of ($Co^{IV}$, $Fe^{IV}$)$O_2$ species with higher valence states[83–87] could be corroborated by the slightly weakened intensity discovered in the first and second shell scatterings between 1.4 V and 1.45 V *vs.* RHE. The changes in oxidation states of Co and Fe (Fig. 4f and Fig. S86b, ESI†) further support our observations about the formation of ($Co^{IV}$, $Fe^{IV}$)$O_2$ species, where the high valence state of $Co^{IV}/Fe^{IV}$ appears above 1.35 V *vs.* RHE. The fitting of *operando* Co K-edge FT-EXAFS spectra (Fig. 4g and Table S10, ESI†) reveals that the structural reconstruction from Co@CoFe–P NBs to (Co, Fe)OOH is accomplished at 1.325 V *vs.* RHE. Compared with the largely delayed formation of CoOOH in the case of Co–P NBs (1.425 V *vs.* RHE), the *operando* XAS results for Co@CoFe–P NBs during the OER confirm that the structural reconstruction is facilitated by Fe substitution.[5,78] The Fe K-edge FT-EXAFS measurements show similar changes in the local coordination environment compared with the Co K-edge (Fig. S86 and Discussion VI, ESI†).

 

**Intrinsic OER mechanism.** According to the *operando* XAS results, we propose that the as-prepared Co@CoFe–P NBs undergo the following dynamically structural reconstructions and evolution of the catalytically active species: (i) appearance of initial Co@CoFe–$P_{6-x}O_x$ species below 0.8 V *vs.* RHE; (ii) formation of (Co@CoFe–$P_{6-x}O_x$)@(Co, Fe)$(OH)_2$@CoOOH from 1.0 to 1.1 V *vs.* RHE; (iii) generation of intermediates of (Co@CoFe–$P_{6-x}O_x$)@(Co, Fe)$(OH)_2$(transient)@(Co, Fe)OOH from 1.2 V to 1.3 V *vs.* RHE; (iv) structural reconstruction of (Co, Fe)OOH accomplished at 1.325 V *vs.* RHE; (v) release of $O_2$ from high valence states of ($Co^{IV}$, $Fe^{IV}$)$O_2$ species with $Co^{IV}$–O–$Fe^{IV}$ configurations above 1.4 V *vs.* RHE; and (vi) structural recovery of (Co, Fe)OOH after the removal of the anodic potential.

**Role of P species in the OER.** To understand the role of P species on the structural reconstruction and on the catalytic OER mechanism, we performed *operando* XAS tests of reference Co–FeOOH under OER conditions (Fig. S87–S90, ESI†). Our *operando* XAS investigations (Discussion VII, ESI†) reveal that the formation of $Co^{III/IV}$–O–$Fe^{III/IV}$ configuration in Co–FeOOH is much more difficult when compared with Co@CoFe–P. With these results at hand, we propose that the main driving forces behind the formation of high-valence active species are highly disordered intermediates during the structural reconstruction of Co@CoFe–P (Fig. 4e–h). This hypothesis can furthermore explain why Co@CoFe–P displays much better OER activity compared with Co–FeOOH (Fig. S91, ESI†).

**Reference chalcogenides as HER and OER catalysts.** It is well-accepted that TMCs also undergo similar underlying structural reconstructions under alkaline conditions compared with those of metal phosphides.[32,39,44] This is due to their intrinsic thermodynamic instability as evident from Pourbaix diagrams, *e.g.* $SO_4^{2-}/S^{2-}$ (0.15 V *vs.* RHE), $SeO_3^{2-}$/Se (0.48 V *vs.* RHE), and $TeO_3^{2-}$/Te (0.44 V *vs.* RHE).[81] Therefore, additional *ex situ* XAS studies of the as-prepared Co–S, Co@CoFe–Se, and Co@CoFe–Te were performed. Our results provide similar observations for the dynamics of the structural reconstructions and the real catalytically active species of the as-investigated TMCs compared with those reported here for TMPs during water splitting (Fig. S92–S95 and Discussion VIII, ESI†).

## RRDE and *operando* Raman investigations

To further explore the dynamic evolution of the structural reconstruction and the real catalytically active species of the as-prepared phosphide-based catalysts during the OER process, rotating ring-disk electrode (RRDE) experiments were performed in Ar saturated 1.0 M KOH (discussion and details in Fig. S96 and S97, ESI†). As illustrated in Fig. S96 and S97 (ESI†), Co–P NBs show similar electrochemical behaviour as Co@CoFe–P NBs. Until $Co^{IV}O_2$ and ($Co^{IV}$, $Fe^{IV}$)$O_2$ are generated as active species, both Co–P NBs and Co@CoFe–P NBs do not show any obvious OER currents (Fig. S96 and S97, ESI†). Almost 100% faradaic efficiency is detected in both samples when the anodic potential reaches 1.525 V and 1.475 V *vs.* RHE, respectively. The RRDE results further verify that the structural reconstruction from phosphides to (oxy)hydroxides is a prerequisite for OER. Moreover, the *in situ* generated high valence states of $Co^{IV}O_2$ and ($Co^{IV}$, $Fe^{IV}$)$O_2$ species are responsible for the OER currents. Furthermore, *operando* Raman studies were carried out to investigate the surface catalytically active species during the HER and OER processes (Fig. S98 and S99, ESI†). As expected, similar vibrations assigned to metal-oxygen bonds are observed during both HER and OER processes. Regarding the HER with Co–P NBs (Fig. S98a, ESI†), two obvious peaks located at around 465 $cm^{-1}$ and 670 $cm^{-1}$ can be ascribed to the $E_g$ and $A_{1g}$ modes of Co–O bonds, respectively.[42,49,88] During the OER process with Co–P NBs (Fig. S98b, ESI†), two new peaks appear at 501 $cm^{-1}$ and 570 $cm^{-1}$, which arise from the $E_g$ vibration of Co–O–Co moieties and the $A_{1g}$ mode of CoOOH, respectively.[42,43,49,88] The *operando* Raman spectra of Co@CoFe–P NBs (Fig. S99, ESI†) also display similar vibration peaks during both HER and OER processes compared with that of Co–P NB, except that an additional peak observed at 725 $cm^{-1}$ is assigned to Fe–O bonds.[74,89–92] The RRDE and *operando* Raman observations in their entirety confirm that the *in situ* reconstructed metal–oxygen configurations play key roles during the water splitting process.

## DFT simulations

To gain further insight into the atomistic catalytic mechanisms, density functional theory (DFT) simulations were carried out for HER using a structure model of the as-prepared phosphide catalysts (see Experimental details in the ESI†). Based on our *ex situ* XPS, RRDE, *operando* XAS, and *operando* Raman studies, the *in situ* reconstructed P–Co–O–Fe–P moieties account for the excellent HER activity in Co@CoFe–P NBs. Herein, to simplify the calculation model, we partially removed one phosphorus atom and replaced it with one oxygen atom to simulate the impact of the *in situ* reconstructed configuration in the HER activity of the as-prepared Co@CoFe–P (denoted as O–Co@CoFe–P). Analyses of the projected density of states (pDOS) and of the metal 3d band centers of the as-proposed models reveal that partial incorporation of oxygen atom in Co@CoFe–P can regulate the energy barriers towards more favorable adsorption of HER intermediates (Fig. S100 and S101 Discussion IX, ESI†).

To explain the catalytic activities in more detail, the adsorption free energies of the H* intermediates ($\Delta G_{H^*}$) for the proposed models were calculated. In general, an ideal HER catalyst should have a $\Delta G_{H^*}$ value near zero to facilitate both the H* adsorption and desorption based on the Sabatier principle.[40,68,93–95] As depicted in Fig. 5a, b and Fig. S100 (ESI†), the calculated $\Delta G_{H^*}$ value at the Co site in Co–P exhibits the most negative value of −0.60 eV among the investigated models, indicating the strongest bonding between Co and H*. Nevertheless, after incorporation of Fe and O into the lattice of Co–P, the calculated $\Delta G_{H^*}$ value is remarkably decreased to −0.42 eV in Co@CoFe–P and −0.40 eV in O–Co@CoFe–P, respectively. Such smaller adsorption energies suggest that Fe substitution can improve the HER activity of Co–P. Besides H* adsorption, the adsorption and dissociation of water molecules are further kinetic barriers for HER under alkaline conditions.[38,40] Therefore, the bonding energies of $H_2O$ molecules adsorbed on Co–P, Co@CoFe–P, and O–Co@CoFe–P were calculated. As shown

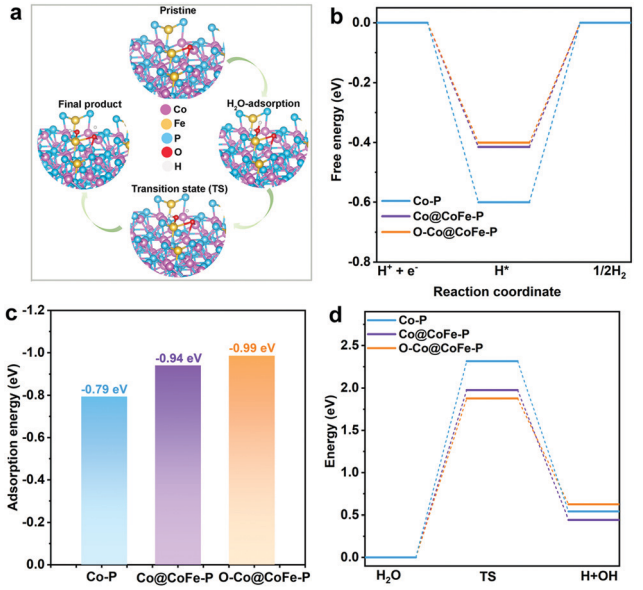


Fig. 5 (a) Optimized adsorption slab models of O–Co@CoFe–P towards HER under alkaline conditions (TS = transition state). (b) Calculated free energy diagrams of H* intermediates adsorbed on three models. (c) Calculated adsorption energy of $H_2O$ molecules. (d) Calculated related reaction energy of water dissociation.

in Fig. 5c, the adsorption of water molecules is more thermodynamically favorable on Co@CoFe–P and O–Co@CoFe–P compared with Co–P, which reflects their lower energy barrier for proton dissociation. The calculations (Fig. 5d) indicate that for Co–P a minimum energy barrier of 2.31 eV must be overcome to dissociate one $H_2O$ molecule, which is higher than those for Co@CoFe–P (1.98 eV) and O–Co@CoFe–P (1.88 eV). It is noteworthy that the active metal site for water adsorption and dissociation is relocated from the Co site in Co–P to the Fe site in Co@CoFe–P, owing to the higher 3d-band center position of Fe compared with Co (Fig. S100d, ESI†). This is in line with *operando* XAS analyses (Fig. 4b and Fig. S82b, ESI†), where the changes in the Fe oxidation state are greater than for Co sites during the HER process. After water dissociation is accomplished, the dissociated proton preferably moves to a neighboring Co site of the P–Co–O–Fe–P moieties to release $H_2$ (Fig. 5a). On combining the above experimental and computational results, we conclude that partial substitution of Co by Fe in Co–P NBs can improve the HER activity by accelerating the water dissociation process and facilitating proton release. During the HER process, the *in situ* reconstructed O–Co@CoFe–P acts as real catalytically active species *via* its P–Co–O–Fe–P moieties. The formation of P–Co–O–Fe–P moieties not only optimizes $\Delta G_{H^*}$ but also facilitates the water dissociation process.

For the OER, we demonstrate that the *in situ* reconstruction into $Co^{IV}$–O–$Fe^{IV}$ moieties plays a pivotal role in the OER activity of Co@CoFe–P NBs. Recent DFT investigations of Co-based materials reveal that the appearance of the oxygen-bridged $Co^{IV}$–O–$Fe^{IV}$ configurations leads to more preferable adsorption energies for OER intermediates (OO* or OOH*) compared with single Co sites or $Co^{IV}$–O–$Co^{IV}$ configurations, thus accounting for the enhanced OER activity of the as-prepared Co@CoFe–P NBs.[80,82–84,96,97]

### Perspectives

Concerning a broader catalyst design impact, our results indicate that anionic substitution strategies are promising to further optimize pnictide- and chalcogenide-based transition metal electrocatalysts for water splitting. The intrinsic thermodynamic properties of materials with different anions (*e.g.* O, P, S, Se, and Te) enable a local electronic regulation of the reconstructed active configurations[12,13] for higher HER performance. Our *operando* results point to the stepwise transformation/oxidation and the subsequent formation of high valence states of metal ions in M–O–M moieties derived from anionic leaching during the OER process. This is regarded as a common denominator of TMCs and TMPs during the OER process. Concerning the advantages of TMCs and TMPs as OER catalysts compared with current operational catalysts based on metal (oxy)hydroxides, we believe that the *in situ* formation of highly disordered structures in TMCs and TMPs is a vital contribution to their higher OER activity (Fig. S87–S91, ESI†). However, the influence of residual pnictide/chalcogenide anions remaining on the surface or in the electrolyte still needs to be clarified in detail as well, especially *via* advanced surface sensitive techniques,[85,96] such as *in situ*/*operando* soft XAS, XPS, and FT-IR techniques.

## Conclusions

In summary, we present a convenient self-templated strategy starting from versatile ZIF-67 nanocube (NC) and yolk–shell ZIF-67@CoFe–PB NC precursors for the preparation of a series of single-shell Co–S, Fe–P and Co–P nanoboxes (NBs), and hierarchically nanostructured Co–S@CoFe–PB, Co@CoFe–O, Co@CoFe–P, Co@CoFe–Se, and Co@CoFe–Te through facile chemical vapor deposition methods.

The as-prepared Co@CoFe–P NBs are highly active and robust electrocatalysts for both hydrogen and oxygen evolution over a wide pH range (0–14). Co@CoFe–P NBs with tailored hierarchical architectures excel through promising catalytic performance with low HER overpotentials (at 10 mA $cm^{-2}$) of 83 mV in 0.5 M $H_2SO_4$, 104 mV in 1.0 M KOH, and 150 mV in 1.0 M PBS, as well as 266 mV in 1.0 M KOH for OER. Inspired by the excellent HER and OER activities of the Co@CoFe–P NBs, we further assembled them as nanostructured bifunctional electrodes for overall water splitting. The as-synthesized Co@CoFe–P NBs provide a current density of 10 mA $cm^{-2}$ at a very low cell voltage of 1.49 V. Most importantly, the device retains current densities of 10 mA $cm^{-2}$, 50 mA $cm^{-2}$, and 100 mA $cm^{-2}$ for over 220 h without a significant decline, thus displaying a high potential for applied industrial electrocatalysis.

To identify the structural HER/OER reconstruction dynamics and the real catalytically active species of the as-prepared Co@CoFe–P NBs and reference Co–P, *operando* XAS and Raman spectra as well as RRDE studies were performed. Our results demonstrate that the active HER species in Co–P and

 

Co@CoFe–P NBs arise from *in situ* reconstructed P–Co–O and P–Co–O–Fe–P configurations with low-valence metal sites ($M^0/M^+$). Moreover, DFT simulations confirm that these *in situ* reconstructed species lower the energy barriers for water dissociation and adsorption of H* intermediates, thereby enhancing the HER activity.

As for OER, we show that the as-prepared Co–P and Co@CoFe–P NBs undergo stepwise structural reconstructions into highly catalytically active $Co^{IV}$–O–$Co^{IV}$ moieties and $Co^{IV}$–O–$Fe^{IV}$ configurations, respectively. Notably, the formation of such reactive $Co^{III/IV}$–O–$Fe^{III/IV}$ configurations is basically suppressed in reference Co–FeOOH under the same conditions, which reveals the specific advantages of phosphide-based catalysts for OER. On a larger scale, *ex situ* studies evidence that a range of as-prepared reference chalcogenides confirm the above trends through closely related general changes in the local electronic structure and coordination environments of their metal centers. Their individual dynamic structural reconstructions and real catalytically active species now remain to be specified with detailed *in situ* monitoring studies.

We present a convenient *operando* tracking approach for the structural reconstruction dynamics and the involved active catalytic species of TMPs during HER and OER. Our results on TMCs furthermore pave the way for future studies on HER in alkaline media *via* anionic substitution strategies to generate optimized reactive A–M–O–M–A (A: P, S, Se, and Te; M: Fe, Co, and Ni) configurations. The emerging design principles for new noble metal-free multifunctional electrocatalysts will expedite the progress of low-cost, applied energy conversion and storage systems.

## Author contributions

G. R. Patzke supervised this project. Y. G. Zhao and G. R. Patzke contributed to the original idea, experimental strategy, and manuscript writing. Y. G. Zhao performed all syntheses, characterization studies, electrochemical performance tests, *operando* XAS tests, and data analyses, and prepared the manuscript. N. C. Dongfang, J. G. Lan, and M. Iannuzzi performed the DFT calculations and data analysis. C. A. Triana helped with the XANES simulations and XAS data analyses. C. Huang and D. Stoian helped with *operando* XAS experiments and data analysis. R. Erni conducted HR-TEM and HAADF-STEM characterization studies. W. C. Wan and J. G. Li helped with data analyses. L. Pan performed the sodium-ion battery tests. P. Zhang assisted with XPS measurements. All authors reviewed and commented on the manuscript before submission.

## Conflicts of interest

There are no conflicts to declare.

## Acknowledgements

Y. G. Zhao, N. C. Dongfang, C. A. Triana, C. Huang, W. C. Wan, J. G. Li, J. G. Lan, M. Iannuzzi, and G. R. Patzke thank the University of Zurich Research Priority Program *Solar Light to Chemical Energy Conversion* (URPP LightChEC) for financial support. G. R. Patzke is grateful to the Swiss National Science Foundation (Sinergia Grant No. CRSII2_160801) for financial support. R. Erni acknowledges funding from the European Research Council (ERC) under the EU Horizon 2020 Research and Innovation Program (Grant agreement no. 681312). The authors acknowledge the assistance and support of the Center for Microscopy and Image Analysis (UZH) in performing scanning electron microscopy experiments. The authors thank Dr W. van Beek and Dr D. Stoian (Swiss-Norwegian Beamline at the European Synchrotron Radiation Facility) for the allocation of synchrotron beamtime and for their support at the BM31 beamline for setting up the *operando* XAS tests. The authors thank Viviane Grange (Department of Chemistry, UZH) for conducting elemental analyses and ICP-MS measurements, and Hanspeter Stalder (Department of Chemistry, UZH) for his help with constructing electrochemical cells for *operando* experiments.

## References

1 M. J. Craig and M. García-Melchor, *Nat. Catal.*, 2020, **3**, 967–968.
2 B. Zhang, L. Wang, Z. Cao, S. M. Kozlov, G. de Arquer, F. Pelayo, C. T. Dinh, J. Li, Z. Wang, X. Zheng, L. Zhang, Y. Wen, O. Voznyy, R. Comin, P. de Luna, T. Regier, W. Bi, E. E. Alp, C.-W. Pao, L. Zheng, Y. Hu, Y. Ji, Y. Li, Y. Zhang, L. Cavallo, H. Peng and E. H. Sargent, *Nat. Catal.*, 2020, **3**, 985–992.
3 J. Wang, S.-J. Kim, J. Liu, Y. Gao, S. Choi, J. Han, H. Shin, S. Jo, J. Kim, F. Ciucci, H. Kim, Q. Li, W. Yang, X. Long, S. Yang, S.-P. Cho, K. H. Chae, M. G. Kim, H. Kim and J. Lim, *Nat. Catal.*, 2021, **4**, 212–222.
4 J. Song, C. Wei, Z.-F. Huang, C. Liu, L. Zeng, X. Wang and Z. J. Xu, *Chem. Soc. Rev.*, 2020, **49**, 2196–2214.
5 E. Fabbri, M. Nachtegaal, T. Binninger, X. Cheng, B.-J. Kim, J. Durst, F. Bozza, T. Graule, R. Schäublin, L. Wiles, M. Pertoso, N. Danilovic, K. E. Ayers and T. J. Schmidt, *Nat. Mater.*, 2017, **16**, 925–931.
6 W. Hao, R. Wu, H. Huang, X. Ou, L. Wang, D. Sun, X. Ma and Y. Guo, *Energy Environ. Sci.*, 2020, **13**, 102–110.
7 K. Jiang, M. Luo, M. Peng, Y. Yu, Y.-R. Lu, T.-S. Chan, P. Liu, F. M. F. de Groot and Y. Tan, *Nat. Commun.*, 2020, **11**, 2701.
8 X. Zheng, B. Zhang, P. de Luna, Y. Liang, R. Comin, O. Voznyy, L. Han, G. de Arquer, F. Pelayo, M. Liu, C. T. Dinh, T. Regier, J. J. Dynes, S. He, H. L. Xin, H. Peng, D. Prendergast, X. Du and E. H. Sargent, *Nat. Chem.*, 2018, **10**, 149–154.
9 Y. Pan, K. Sun, Y. Lin, X. Cao, Y. Cheng, S. Liu, L. Zeng, W.-C. Cheong, D. Zhao, K. Wu, Z. Liu, Y. Liu, D. Wang, Q. Peng, C. Chen and Y. Li, *Nano Energy*, 2019, **56**, 411–419.
10 K. Jiang, B. Liu, M. Luo, S. Ning, M. Peng, Y. Zhao, Y.-R. Lu, T.-S. Chan, F. M. F. de Groot and Y. Tan, *Nat. Commun.*, 2019, **10**, 1743.
11 S.-F. Hung, Y. Zhu, G.-Q. Tzeng, H.-C. Chen, C.-S. Hsu, Y.-F. Liao, H. Ishii, N. Hiraoka and H. M. Chen, *ACS Energy Lett.*, 2019, **4**, 2813–2820.

12 Y. Zhu, H.-C. Chen, C.-S. Hsu, T.-S. Lin, C.-J. Chang, S.-C. Chang, L.-D. Tsai and H. M. Chen, *ACS Energy Lett.*, 2019, **4**, 987–994.
13 Y. Shi, M. Li, Y. Yu and B. Zhang, *Energy Environ. Sci.*, 2020, **13**, 4564–4582.
14 D. Cao, D. Liu, S. Chen, O. A. Moses, X. Chen, W. Xu, C. Wu, L. Zheng, S. Chu, H. Jiang, C. Wang, B. Ge, X. Wu, J. Zhang and L. Song, *Energy Environ. Sci.*, 2021, **14**, 906–915.
15 J. Song, *ACS Energy Lett.*, 2017, **2**, 1937–1938.
16 Y. Zhang, L. Gao, E. J. M. Hensen and J. P. Hofmann, *ACS Energy Lett.*, 2018, **3**, 1360–1365.
17 Y. Zhang and L. Song, *ChemCatChem*, 2020, **12**, 3621–3638.
18 A. Sivanantham, P. Ganesan, A. Vinu and S. Shanmugam, *ACS Catal.*, 2020, **10**, 463–493.
19 A. Indra, P. W. Menezes, I. Zaharieva, H. Dau and M. Driess, *J. Mater. Chem. A*, 2020, **8**, 2637–2643.
20 K. Fan, H. Zou, Y. Lu, H. Chen, F. Li, J. Liu, L. Sun, L. Tong, M. F. Toney, M. Sui and J. Yu, *ACS Nano*, 2018, **12**, 12369–12379.
21 M. Wang, C.-L. Dong, Y.-C. Huang and S. Shen, *ACS Catal.*, 2020, **10**, 1855–1864.
22 S. Sun, X. Zhou, B. Cong, W. Hong and G. Chen, *ACS Catal.*, 2020, **10**, 9086–9097.
23 K. Xu, Y. Sun, X. Li, Z. Zhao, Y. Zhang, C. Li and H. J. Fan, *ACS Mater. Lett.*, 2020, **2**, 736–743.
24 Y. Shi, W. Du, W. Zhou, C. Wang, S. Lu, S. Lu and B. Zhang, *Angew. Chem., Int. Ed.*, 2020, **59**, 22470–22474.
25 J.-Y. Zhang, Y. Yan, B. Mei, R. Qi, T. He, Z. Wang, W. Fang, S. Zaman, Y. Su, S. Ding and B. Y. Xia, *Energy Environ. Sci.*, 2021, **14**, 365–373.
26 J. Huang, Y. Li, Y. Zhang, G. Rao, C. Wu, Y. Hu, X. Wang, R. Lu, Y. Li and J. Xiong, *Angew. Chem., Int. Ed.*, 2019, **58**, 17458–17464.
27 Y. Dou, C.-T. He, L. Zhang, H. Yin, M. Al-Mamun, J. Ma and H. Zhao, *Nat. Commun.*, 2020, **11**, 1664.
28 X. Zheng, X. Han, Y. Cao, Y. Zhang, D. Nordlund, J. Wang, S. Chou, H. Liu, L. Li, C. Zhong, Y. Deng and W. Hu, *Adv. Mater.*, 2020, **32**, 2000607.
29 T. Zhao, X. Shen, Y. Wang, R. K. Hocking, Y. Li, C. Rong, K. Dastafkan, Z. Su and C. Zhao, *Adv. Funct. Mater.*, 2021, **31**, 2100614.
30 W. Zhao, C. Zhang, F. Geng, S. Zhuo and B. Zhang, *ACS Nano*, 2014, **8**, 10909–10919.
31 Z. Wu, Q. Gan, X. Li, Y. Zhong and H. Wang, *J. Phys. Chem. C*, 2018, **122**, 2848–2853.
32 H. Zhang, W. Zhou, J. Dong, X. F. Lu and X. W. Lou, *Energy Environ. Sci.*, 2019, **12**, 3348–3355.
33 Y. Zhao, J. Zhang, Y. Xie, B. Sun, J. Jiang, W.-J. Jiang, S. Xi, H. Y. Yang, K. Yan, S. Wang, X. Guo, P. Li, Z. Han, X. Lu, H. Liu and G. Wang, *Nano Lett.*, 2021, **21**, 823–832.
34 Z.-F. Huang, J. Song, K. Li, M. Tahir, Y.-T. Wang, L. Pan, L. Wang, X. Zhang and J.-J. Zou, *J. Am. Chem. Soc.*, 2016, **138**, 1359–1365.
35 C. Zhang, Y. Huang, Y. Yu, J. Zhang, S. Zhuo and B. Zhang, *Chem. Sci.*, 2017, **8**, 2769–2775.
36 C. Zhang, Y. Shi, Y. Yu, Y. Du and B. Zhang, *ACS Catal.*, 2018, **8**, 8077–8083.
37 S. Zhuo, Y. Shi, L. Liu, R. Li, L. Shi, D. H. Anjum, Y. Han and P. Wang, *Nat. Commun.*, 2018, **9**, 3132.
38 Q. Fu, X. Wang, J. Han, J. Zhong, T. Zhang, T. Yao, C. Xu, T. Gao, S. Xi, C. Liang, L. Xu, P. Xu and B. Song, *Angew. Chem., Int. Ed.*, 2021, **60**, 259–267.
39 X. Liu, Y. Yao, H. Zhang, L. Pan, C. Shi, X. Zhang, Z.-F. Huang and J.-J. Zou, *ACS Sustainable Chem. Eng.*, 2020, **8**, 17828–17838.
40 D. Zhao, K. Sun, W.-C. Cheong, L. Zheng, C. Zhang, S. Liu, X. Cao, K. Wu, Y. Pan, Z. Zhuang, B. Hu, D. Wang, Q. Peng, C. Chen and Y. Li, *Angew. Chem., Int. Ed.*, 2020, **59**, 8982–8990.
41 Y. Zhu, J. Wang, H. Chu, Y.-C. Chu and H. M. Chen, *ACS Energy Lett.*, 2020, **5**, 1281–1291.
42 J. Liu, Q. Hu, Y. Wang, Z. Yang, X. Fan, L.-M. Liu and L. Guo, *Proc. Natl. Acad. Sci. U. S. A.*, 2020, **117**, 21906–21913.
43 J. N. Hausmann, S. Mebs, K. Laun, I. Zebger, H. Dau, P. W. Menezes and M. Driess, *Energy Environ. Sci.*, 2020, **13**, 3607–3619.
44 L. J. Enman, M. B. Stevens, M. H. Dahan, M. R. Nellist, M. C. Toroker and S. W. Boettcher, *Angew. Chem., Int. Ed.*, 2018, **57**, 12840–12844.
45 J. Timoshenko and B. Roldan Cuenya, *Chem. Rev.*, 2021, **121**, 882–961.
46 B.-J. Kim, E. Fabbri, D. F. Abbott, X. Cheng, A. H. Clark, M. Nachtegaal, M. Borlaf, I. E. Castelli, T. Graule and T. J. Schmidt, *J. Am. Chem. Soc.*, 2019, **141**, 5231–5240.
47 S. Song, J. Zhou, X. Su, Y. Wang, J. Li, L. Zhang, G. Xiao, C. Guan, R. Liu, S. Chen, H.-J. Lin, S. Zhang and J.-Q. Wang, *Energy Environ. Sci.*, 2018, **11**, 2945–2953.
48 L. Cao, Q. Luo, W. Liu, Y. Lin, X. Liu, Y. Cao, W. Zhang, Y. Wu, J. Yang, T. Yao and S. Wei, *Nat. Catal.*, 2019, **2**, 134–141.
49 Z. Kou, Y. Yu, X. Liu, X. Gao, L. Zheng, H. Zou, Y. Pang, Z. Wang, Z. Pan, J. He, S. J. Pennycook and J. Wang, *ACS Catal.*, 2020, **10**, 4411–4419.
50 W. Wan, C. A. Triana, J. Lan, J. Li, C. S. Allen, Y. Zhao, M. Iannuzzi and G. R. Patzke, *ACS Nano*, 2020, **14**, 13279–13293.
51 Z. Xiao, Y.-C. Huang, C.-L. Dong, C. Xie, Z. Liu, S. Du, W. Chen, D. Yan, L. Tao, Z. Shu, G. Zhang, H. Duan, Y. Wang, Y. Zou, R. Chen and S. Wang, *J. Am. Chem. Soc.*, 2020, **142**, 12087–12095.
52 F. Dionigi, Z. Zeng, I. Sinev, T. Merzdorf, S. Deshpande, M. B. Lopez, S. Kunze, I. Zegkinoglou, H. Sarodnik, D. Fan, A. Bergmann, J. Drnec, J. F. de Araujo, M. Gliech, D. Teschner, J. Zhu, W.-X. Li, J. Greeley, B. R. Cuenya and P. Strasser, *Nat. Commun.*, 2020, **11**, 2522.
53 Y. Zhou, S. Sun, J. Song, S. Xi, B. Chen, Y. Du, A. C. Fisher, F. Cheng, X. Wang, H. Zhang and Z. J. Xu, *Adv. Mater.*, 2018, **30**, 1802912.
54 Z.-F. Huang, J. Song, Y. Du, S. Xi, S. Dou, J. M. V. Nsanzimana, C. Wang, Z. J. Xu and X. Wang, *Nat. Energy*, 2019, **4**, 329–338.
55 Y. Zhao, W. Wan, Y. Chen, R. Erni, C. A. Triana, J. Li, C. K. Mavrokefalos, Y. Zhou and G. R. Patzke, *Adv. Energy Mater.*, 2020, **10**, 2002228.

 

56 Y. Duan, J. Y. Lee, S. Xi, Y. Sun, J. Ge, S. J. H. Ong, Y. Chen, S. Dou, F. Meng, C. Diao, A. C. Fisher, X. Wang, G. G. Scherer, A. Grimaud and Z. J. Xu, *Angew. Chem., Int. Ed.*, 2021, **60**, 7418–7425.
57 H. Hu, B. Y. Guan and X. W. Lou, *Chem*, 2016, **1**, 102–113.
58 H. Liu, J. Guan, S. Yang, Y. Yu, R. Shao, Z. Zhang, M. Dou, F. Wang and Q. Xu, *Adv. Mater.*, 2020, **32**, 2003649.
59 X. Wang, L. Yu, B. Y. Guan, S. Song and X. W. Lou, *Adv. Mater.*, 2018, **30**, 1801211.
60 Z. Li, X. Zhang, Y. Kang, C. C. Yu, Y. Wen, M. Hu, D. Meng, W. Song and Y. Yang, *Adv. Sci.*, 2021, **8**, 2002631.
61 H. Hu, L. Han, M. Yu, Z. Wang and X. W. Lou, *Energy Environ. Sci.*, 2016, **9**, 107–111.
62 Y. Zhao, C. K. Mavrokefalos, P. Zhang, R. Erni, J. Li, C. A. Triana and G. R. Patzke, *Chem. Mater.*, 2020, **32**, 1371–1383.
63 W. Wang, H. Yan, U. Anand and U. Mirsaidov, *J. Am. Chem. Soc.*, 2021, **143**, 1854–1862.
64 G. Zhang, Y. Li, X. Xiao, Y. Shan, Y. Bai, H.-G. Xue, H. Pang, Z. Tian and Q. Xu, *Nano Lett.*, 2021, **21**, 3016–3025.
65 J. Wang, Y. Gao, H. Kong, J. Kim, S. Choi, F. Ciucci, Y. Hao, S. Yang, Z. Shao and J. Lim, *Chem. Soc. Rev.*, 2020, **49**, 9154–9196.
66 Y. Pan, K. Sun, S. Liu, X. Cao, K. Wu, W.-C. Cheong, Z. Chen, Y. Wang, Y. Li, Y. Liu, D. Wang, Q. Peng, C. Chen and Y. Li, *J. Am. Chem. Soc.*, 2018, **140**, 2610–2618.
67 Z. Li, W. Niu, Z. Yang, A. Kara, Q. Wang, M. Wang, M. Gu, Z. Feng, Y. Du and Y. Yang, *Energy Environ. Sci.*, 2020, **13**, 3110–3118.
68 Z. Chen, M. Chen, X. Yan, H. Jia, B. Fei, Y. Ha, H. Qing, H. Yang, M. Liu and R. Wu, *ACS Nano*, 2020, **14**, 6968–6979.
69 Y. Dong, T. Tian, C. Xu, K. Ma, W. Sun and Y. Ding, *J. Catal.*, 2020, **382**, 13–21.
70 P. Hou, D. Li, N. Yang, J. Wan, C. Zhang, X. Zhang, H. Jiang, Q. Zhang, L. Gu and D. Wang, *Angew. Chem., Int. Ed.*, 2021, **60**, 6926–6931.
71 F. M. F. de Groot, S. Pizzini, A. Fontaine, K. Hämäläinen, C. C. Kao and J. B. Hastings, *Phys. Rev. B: Condens. Matter Mater. Phys.*, 1995, **51**, 1045–1052.
72 A. P. Grosvenor, R. G. Cavell and A. Mar, *J. Solid State Chem.*, 2007, **180**, 2702–2712.
73 A. P. Grosvenor, R. G. Cavell and A. Mar, *J. Solid State Chem.*, 2008, **181**, 2549–2558.
74 J. Yu, Q. Cao, Y. Li, X. Long, S. Yang, J. K. Clark, M. Nakabayashi, N. Shibata and J.-J. Delaunay, *ACS Catal.*, 2019, **9**, 1605–1611.
75 J. Yu, J. Wang, X. Long, L. Chen, Q. Cao, C. Qiu, J. Lim and S. Yang, *Adv. Energy Mater.*, 2021, **11**, 2002731.
76 M. Zheng, Y. Ding, L. Yu, X. Du and Y. Zhao, *Adv. Funct. Mater.*, 2017, **27**, 1605846.
77 B. Pattengale, Y. Huang, X. Yan, S. Yang, S. Younan, W. Hu, Z. Li, S. Lee, X. Pan, J. Gu and J. Huang, *Nat. Commun.*, 2020, **11**, 4114.
78 T. Wu, S. Sun, J. Song, S. Xi, Y. Du, B. Chen, W. A. Sasangka, H. Liao, C. L. Gan, G. G. Scherer, L. Zeng, H. Wang, H. Li, A. Grimaud and Z. J. Xu, *Nat. Catal.*, 2019, **2**, 763–772.
79 L. Bai, C.-S. Hsu, D. T. L. Alexander, H. M. Chen and X. Hu, *J. Am. Chem. Soc.*, 2019, **141**, 14190–14199.
80 J. Zhou, Y. Wang, X. Su, S. Gu, R. Liu, Y. Huang, S. Yan, J. Li and S. Zhang, *Energy Environ. Sci.*, 2019, **12**, 739–746.
81 G. K. Schweitzer and L. L. Pesterfield, *The Aqueous Chemistry of the Elements*, Oxford University Press, 2010.
82 A. Bergmann, T. E. Jones, E. Martinez Moreno, D. Teschner, P. Chernev, M. Gliech, T. Reier, H. Dau and P. Strasser, *Nat. Catal.*, 2018, **1**, 711–719.
83 A. Moysiadou, S. Lee, C.-S. Hsu, H. M. Chen and X. Hu, *J. Am. Chem. Soc.*, 2020, **142**, 11901–11914.
84 J. T. Mefford, Z. Zhao, M. Bajdich and W. C. Chueh, *Energy Environ. Sci.*, 2020, **13**, 622–634.
85 J. T. Mefford, A. R. Akbashev, M. Kang, C. L. Bentley, W. E. Gent, H. D. Deng, D. H. Alsem, Y.-S. Yu, N. J. Salmon, D. A. Shapiro, P. R. Unwin and W. C. Chueh, *Nature*, 2021, **593**, 67–73.
86 M. Risch, F. Ringleb, M. Kohlhoff, P. Bogdanoff, P. Chernev, I. Zaharieva and H. Dau, *Energy Environ. Sci.*, 2015, **8**, 661–674.
87 J. G. McAlpin, Y. Surendranath, M. Dinca, T. A. Stich, S. A. Stoian, W. H. Casey, D. G. Nocera and R. D. Britt, *J. Am. Chem. Soc.*, 2010, **132**, 6882–6883.
88 W. Zheng, M. Liu and L. Y. S. Lee, *ACS Catal.*, 2020, **10**, 81–92.
89 S. Jiao, X. Fu, S. Wang and Y. Zhao, *Energy Environ. Sci.*, 2021, **14**, 1722–1770.
90 S. Réguer, D. Neff, L. Bellot-Gurlet and P. Dillmann, *J. Raman Spectrosc.*, 2007, **38**, 389–397.
91 L. Bai, S. Lee and X. Hu, *Angew. Chem., Int. Ed.*, 2021, **60**, 3095–3103.
92 B. Chakraborty, R. Beltrán-Suito, J. N. Hausmann, S. Garai, M. Driess and P. W. Menezes, *Adv. Energy Mater.*, 2020, **10**, 2001377.
93 Y. An, X. Long, M. Ma, J. Hu, H. Lin, D. Zhou, Z. Xing, B. Huang and S. Yang, *Adv. Energy Mater.*, 2019, **9**, 1901454.
94 H. Feng, L. Tang, G. Zeng, J. Yu, Y. Deng, Y. Zhou, J. Wang, C. Feng, T. Luo and B. Shao, *Nano Energy*, 2020, **67**, 104174.
95 Z. Wang, Z. Lin, J. Deng, S. Shen, F. Meng, J. Zhang, Q. Zhang, W. Zhong and L. Gu, *Adv. Energy Mater.*, 2021, **11**, 2003023.
96 J. Li, C. A. Triana, W. Wan, D. P. Adiyeri Saseendran, Y. Zhao, S. E. Balaghi, S. Heidari and G. R. Patzke, *Chem. Soc. Rev.*, 2021, **50**, 2444–2485.
97 N. Zhang, X. Feng, D. Rao, X. Deng, L. Cai, B. Qiu, R. Long, Y. Xiong, Y. Lu and Y. Chai, *Nat. Commun.*, 2020, **11**, 4066.